Astronomy & Astrophysics manuscript no. IRMHDpaperdraft
September 6, 2010

Production of Elephant Trunks in HII Regions by Radiation-Magnetohydrodynamic Instabilities

Katharina M. Fierlinger[1,2], Matthias Gritschneder[3], and Mark R. Krumholz[4] ⋆

[1] Excellence Cluster Universe, Boltzmannstr. 2, 85748 Garching, Germany
[2] Universitätssternwarte München, Scheinerstr. 1, 81679 Munich, Germany e-mail: kfierlin@usm.lmu.de
[3] The Kavli Institute for Astronomy and Astrophysics, Peking University Yi He Yuan Lu 5, Hai Dian Qu Beijing 100871, P. R. China e-mail: gritschneder@pku.edu.cn
[4] Department of Astronomy & Astrophysics, University of California, Santa Cruz, CA 95060, USA e-mail: krumholz@ucolick.org

Received month dd, 2010; accepted month dd, yyyy

ABSTRACT

Context. Recent SPH and grid code simulations showed, that ionizing radiation can amplify overdensities in turbulent molecular clouds and produce molecular pillars. The relevance of magnetic fields for the structure and stability of molecular clouds is still under discussion.
Aims. We investigate whether an ionization front hitting a medium with small distortions of the magnetic field can produce the observed pillar-like structures in star forming regions (e.g. Eagle Nebula).
Methods. Numerical MHD simulations with the Athena 2.0 grid code with ionizing radiation were performed.
Results. It turns out that the ionizing radiation drives a shock wave into the cold magnetized cloud and amplifies overdensities seeded by Alfvén waves.
Conclusions. Alfvén waves can be seeds for molecular pillars. However, the magnetic field in structures created by Alfvén waves makes these regions hostile to star formation.

Key words. ISM: bubbles – Stars: winds, outflows – Magnetohydrodynamics – Instabilities – Methods: numerical – ISM: kinematics and dynamics

1. Introduction

Recent observations provide unprecedented data of interactions between cold magnetized molecular clouds and UV light from massive stars. In such regions molecular pillars can be found. Famous prototypical examples of these structures are the so called "pillars of creation" (Guarcello et al. 2010) in the Eagle nebula. Comparing the size of the "pillars of creation" to structures in RCW 120 (Deharveng et al. 2005, 2009) and the Carina nebula (Smith et al. 2010) illustrates, that molecular pillars can also be significantly smaller or larger than the ones in the Eagle nebula.

Other well known examples of ionizing radiation interacting with cold molecular gas are Vulpecula OB1 (Billot et al. 2010), the Orion cometary clouds (Stanke et al. 2002), the Omega Nebula (Zhao et al. 2009),the 30 Doradus nebula (Walborn et al. 2002), the Horsehead nebula (Ward-Thompson et al. 2006), and the so called elephant trunk (Ikeda et al. 2008).

By now, molecular pillars of various sizes have been found, however, they are always found on the edges of HII-regions. Typically they display a clear head to tail structure (Sugitani et al. 2002) with the dense head pointing towards an ionizing source. Many molecular pillars also show signs of star formation at their tips. Near-infrared polarimetry of the Eagle Nebula (Sugitani et al. 2007) suggests that the magnetic field in the pillars does not follow the global field pattern. Shock velocities of a few km/s can be inferred from age difference of stars (Ikeda et al. 2008). This morphology of molecular pillars is suggestive of highly turbulent structures created by feedback of UV-radiation and winds of massive stars. Elmegreen et al. (1995) proposed that molecular pillars could be swept up and collapsed material.

Smooth particle hydrodynamic (SPH) simulations (Gritschneder et al. 2009a,b) showed that the interplay of ionizing radiation and turbulent molecular clouds can indeed lead to the creation of molecular pillars. In the simulations of Gritschneder et al. (2009a,b) molecular pillars were seeded by overdensities caused by turbulence. The influence of magnetic fields on the formation of molecular pillars has not been studied. For a recent review on the problems with magnetic fields in SPH simulations see e.g. Price & Bate (2010). However magnetic fields are known to exist in molecular clouds (MCs) (Li et al. 2010) and to stabilize them (Tomisaka et al. 1988). In this work we use a grid code to investigate whether taking into account the presence of magnetic fields in the molecular clouds changes the picture of pillar formation as presented in Gritschneder et al. (2009a,b).

The structure of an ionization front is modified by the presence of a magnetic field, as this causes an increase in the number of wave families that can propagate. For example when an ionization front hits a magnetized molecular cloud, it can drive a magneto sonic wave into the cloud. This leads to qualitatively new phenomena compared to the field free case because the magneto sonic wave will cause a widening shock front and reduce the shock strength. Analytical one-dimensional studies of ionization fronts interacting with a magnetized medium have been presented by Redman et al. (1998); Williams et al. (2000)

⋆ Authors in alphabetical order

γ	5/3	specific heats ratio (C_p/C_v)
$n_{\rm H}$	100	[particles/cm3] initial density
$c_{\rm s}$	2.e4	[cm/s] 0.2 km/s, initial sound speed in the neutral gas
flux	1.e9	[photons/s/cm2] ionizing flux (O-star in 10 pc distance)
$B_{\rm x}$	0	[Gauss/ $\sqrt{4\pi}$]
$B_{\rm y}$	2.82e-6	magnetic field vector
$B_{\rm z}$	0	= (0,10 [μGauss],0)
$k_{\rm y}$	[01234]	wave lengths of the perturbation per parsec
amp	[0125]	amplitude of the perturbation (e.g. 5: $B_{\rm x} = 5\% B_{\rm y}$ fluctuation)

Table 1. Initial conditions used in the simulations (if different IC were used, this is mentioned in the text).

perturbation	$B_{\rm y}$ [μG]	resolution	section
none	0,1,5,10	2x, 1x, 0.5x	3.1
ρ	0,1,5,10	2x, 1x, 0.5x	3.2
ρ, E	0,1,5,10	2x, 1x, 0.5x	3.2
$B_{\rm x}$	0,1,5,10	2x, 1x, 0.5x	3.3
$B_{\rm x}, v_{\rm x}$	0,1,5,10	2x, 1x, 0.5x	3.4
$B_{\rm x}, v_{\rm x}, B_{\rm y}, v_{\rm y}$	0,1,5,10	2x, 1x, 0.5x	3.5

Table 2. List of setups: sinusoidally perturbed quantities, strength of the background magnetic field, resolution with respect to the "standard" resolution of $128 \times 64 \times 2$ cells, section of the report introducing this type of models

alpha_C	4.e-3	Carbon mass fraction
e_gamma	3.84522e-12	[erg] 2.4 eV Energy added to gas by a single photo ionization
k_B	1.38062e-16	[erg/K] Boltzmann's constant
m_H	2.34e-24	[g] Mean mass per H nucleus
mu	3.9e-24	[g] not 2.34e-24 because it's atomic hydrogen, Mean particle mass in neutral gas
sigma_ph	6.3e-18	[cm2] Photo ionization cross section
time_unit	1	[1 year = 31 556 926 seconds] Number of seconds in one code time
tceil	1.e5	[K] max. temperature
tfloor	10	[K] min. temperature
max_de_iter	0.1	Maximum change in total gas energy per iteration
max_de_therm_iter	0.1	Maximum change in gas thermal energy per iteration
max_dx_iter	0.1	Maximum change in ion fraction per iteration
max_de_step	4	Maximum change in total gas energy per hydro step
max_de_therm_step	4	Maximum change in gas thermal energy per hydro step
max_dx_step	4	Maximum change in total gas energy per hydro step
maxiter	500	Maximum number of sub-cycle iterations allowed
min_tree_level	2	Minimum level for ray tree

Table 3. Runtime parameters, details on the ionizing radiation run time parameters can be found in Krumholz et al. (2007).

and Williams & Dyson (2001). Carlqvist et al. (2003) have treated the two-dimensional case with quasi-empirical models and Henney et al. (2009) investigated the three dimensional case numerically.

Further, we investigated if in the presence of a magnetic field, ionizing radiation (IR) is able to produce pillars from initial density perturbations with smaller amplitudes than in the unmagnetized case. There is a bunch of interesting question connected to the smallest seed for pillars: via Alfvén waves, pillars can be created from magnetized clouds without seeding density perturbations at all, but can such seeds lead to pillars with the observed field alignment? Tomisaka et al. (1988) pointed out the strong stabilizing effect of magnetic fields in molecular clouds and introduced the flux to mass ratio ($M_\Phi = 0.12 \frac{\Phi_{\rm B}}{\sqrt{G}}$) to quantify this stabilizing effect. Thus, we also checked if different types of seeds made the pillars more or less prone to star formation.

By studying the process of molecular pillar formation, the interplay of ionizing radiation, turbulence and magnetic fields can be deduced. This can be crucial to our physical understanding of the Giant Molecular Cloud (GMC) lifetimes and star formation: GMCs in the present day universe are gravitationally bound, survive a few crossing times and convert only a few percent of their mass into stars. Thus, they have to be supported by internal feedback. But the turbulence, which can support the clouds against gravitational collapse, decays rather quickly and has to be driven (e.g. by stellar winds, ionizing radiation or supernova explosions).

Since GMCs are subject to MHD effects because the magnetic pressure exceeds the thermal pressure and the magnetic energy is comparable to kinetic and gravitational energy, it is interesting to probe the importance of magnetic fields in the creation molecular pillars. If new types of magnetic ionization front instabilities can be discovered this could help to explain the observed amount of turbulence in GMGs.

2. Simulations

The simulations have been performed with the ionizing radiation version of the Athena 2.0 code (Krumholz et al. 2007; Gardiner & Stone 2005, 2008; Stone et al. 2008; Stone & Gardiner 2009). This code solves the equations of multi-species ideal MHD including radiative heating and cooling and chemical evolution terms. More precicely, the equations for the conservation of mass, momentum, and energy are eq. 1, eq. 2, and eq. 4. Magnetic flux freezing leads to eq. 3, the mass of neutral gas is only altered by ionizations and recombinations eq. 5 and the non-existence of magnetic monopoles is used in eq 6. Total heating an cooling are described by eq. 7 and eq. 8.

$$\frac{\partial \rho}{\partial t} + \nabla \cdot (\rho \mathbf{v}) = 0 \quad (1)$$

$$\frac{\partial}{\partial t}(\rho \mathbf{v}) + \nabla \cdot (\rho \mathbf{v}\mathbf{v} - \mathbf{B}\mathbf{B}) + \nabla P^* = 0 \quad (2)$$

$$\frac{\partial \mathbf{B}}{\partial t} + \nabla \cdot (\mathbf{v}\mathbf{B} - \mathbf{B}\mathbf{v}) = 0 \quad (3)$$

$$\frac{\partial E}{\partial t} + \nabla \cdot \left[(E + P^*)\mathbf{v} - \mathbf{B}(\mathbf{B} \cdot \mathbf{v})\right] = \mathcal{G} - \mathcal{L} \quad (4)$$

$$\frac{\partial \rho_n}{\partial t} + \nabla \cdot (\rho_n \mathbf{v}) = \mathcal{R} - \mathcal{I} \quad (5)$$

$$\nabla \cdot \mathbf{B} = 0 \quad (6)$$

$$\mathcal{G} = e_\Gamma \sigma n_H \sum_n \frac{s_n}{4\pi |\mathbf{x} - \mathbf{x}_n|^2} e^{-\tau(\mathbf{x}, \mathbf{x}_n)} + n_H \Gamma_{\rm KI} \quad (7)$$

$$\mathcal{L} = \Lambda_{\rm KI}(T) n_H^2 + \Lambda_{\rm rec}(T) n_e n_{H^+} + \Lambda_{\rm ion-ff}(T) n_e n_{H^+} \quad (8)$$

with

$\mathbf{v}$	gas speed [cm/s]
$\mathbf{B}$	magnetic field vector [Gauss/ $\sqrt{4\pi}$]
ρ	total density [g/cm^3]
ρ_n	density of neutral species[g/cm^3]
ϵ	gas thermal energy density [erg/cm^3]
E	total energy density [erg/cm^3] without atomic or molecular binding energies $E \equiv \epsilon + \rho\frac{\mathbf{v}\cdot\mathbf{v}}{2} + \frac{\mathbf{B}\cdot\mathbf{B}}{2}$
P^*	total pressure [dyn/cm^2], $P + (\mathbf{B}\cdot\mathbf{B})/2$
P	gas thermal pressure [dyn/cm^2]
$\mathcal{R}$	recombination rate [g/s/cm^3]
$\mathcal{I}$	ionization rate [g/s/cm^3]
$\mathcal{G}$	total radiative heating rate [erg/s/cm^3]
$\mathcal{L}$	total radiative cooling rate [erg/s/cm^3]
$\Gamma_{\rm KI}$	heating following the Koyama & Inutsuka curve
$\Lambda_{\rm KI}$	cooling following the Koyama & Inutsuka curve
$\Lambda_{\rm rec}$	cooling from recombinations
$\Lambda_{\rm ion-ff}$	cooling from ion-neutral collisions and free-free emission in ionized gas

We used ideal MHD, adiabatic EOS for ideal gas ($P = (\gamma - 1)\epsilon$), monoatomic gas ($\gamma = 5/3$), 2nd order, Roe solver, plane parallel ionizing radiation, efficient radiative cooling with solar metalicity and no gravitation.

The standard resolution of the simulations was $128 \times 64 \times 2$ cells for a box of 2 pc $\times$1 pc $\times$1/32 pc. Higher/lower resolutions were used for convergence tests. Details on these tests can be found in section 4.1. Runs with no y-dependence of the initial conditions were also computed with a lower number of cells in y (and consequently with a lower box depth in y, since the individual cells were cubic). Comparing these results with the same runs using $128 \times 64 \times 2$ cells showed that the results did not depend on the box depth.

A mean mass per H nucleus ($m_{\rm H}$) of 2.34×10^{-24} g and a mean particle mass in the neutral gas (μ) of 3.9×10^{-24} g (atomic hydrogen) were chosen for the molecular cloud. The simulation started with an initial density of 100 particles per cubic centimeter, an initial temperature of 10 Kelvin and a magnetic field strength of 10 μGauss.

Characteristic velocities in the simulations were (1) the sound speed in the ionized part ($T_i = 10^4$ K, $c_i = \sqrt{\frac{k_{\rm B}T}{m_{\rm H}}} \sim 8$ km/s because of the ionizing radiation the sound speed in the HII rather isothermal than adiabatic $c_i = \sqrt{\frac{\gamma k_{\rm B}T}{m_{\rm H}}}$), (2) the Alfvén speed ($v_a = \frac{B}{\sqrt{4\pi\rho}} \sim 2$ km/s) and (3) the sound speed in the neutral part ($c_s = \sqrt{\frac{k_{\rm B}T}{\mu}} \sim 0.2$ km/s due to the efficient cooling the sound speed inside the molecular cloud is rather isothermal than adiabatic $c_s = \sqrt{\frac{\gamma k_{\rm B}T}{\mu}}$).

Thus the relevant velocities were well separated ($c_i \gg v_a \gg c_s$) and the fast magneto-sonic velocity is:

$$\frac{\omega^2}{k^2} = \frac{v_a^2 + c_s^2}{2} \pm \sqrt{\left(\frac{v_a^2 + c_s^2}{2}\right)^2 - c_s^2 v_a^2 \cos\Theta} \quad . \tag{9}$$

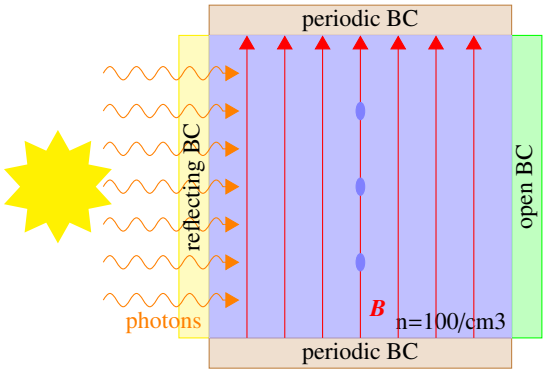

Fig. 1. The toy model for our study of instabilities caused by an ionization front propagating into a magnetized medium is a box with plane parallel radiation from the low x side and a magnetic field along the y direction. Instabilities were triggered by perturbing the magnetic field, momenta or the density (for details see section 3.1 to 3.5).

The parameters are:

ω	angular frequency of the wave
k	wave number
Θ	angle between magnetic field and wave vector
c_s	sound speed [cm/s]
v_a	Alfvén speed ($\frac{B}{\sqrt{4\pi\rho}}$) [cm/s]
B	magnetic field strength [Gauss]
ρ	density [g/cm^3]

The fast magneto-sonic velocity perpendicular to the field ($\cos\Theta = 0$) can catch up with the ionization front.

A homogeneous plane parallel photon flux (f) of 10^9 [photons/cm^2/s] enters the box at the low x side (see fig. 1). This corresponds to the flux of ionizing photons from an O-star in a distance of 10 pc.

Since the radiation enters the box from left side (-x), the simulations use a reflecting boundary condition near the source (-x), outflow boundary condition on the right side (+x), and periodic boundary conditions at all other boundaries (y,z).

3. Results

In this section the propagation of the ionization front and the regions in which overdensities start to build up are discussed for different pillar-formation-seeds. In our simulations we excited different kinds of waves inside the cold, magnetized molecular cloud in order to check, in which respect the overdensities which are created by these distinct waves differ. The "standard" initial conditions for the simulations are summarized in tab. 1. Tab. 2 contains an overview of the different types of perturbations of these initial conditions and the run-time parameters can be found in tab. 3.

3.1. Homogeneous medium

In the zero-field case with homogeneous density the propagation of the ionization front (IF) can be fit with Shu's approximation (Shu 1992). The initial Strömgren sphere ($R_{\rm Strömgren}$) is defined as the radius of the area in which the recombination rate balances

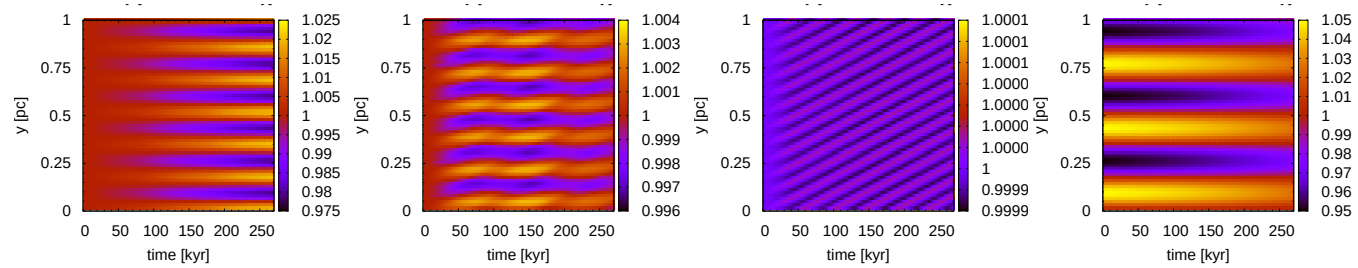

Fig. 4. Evolution of the density in cells which are not reached by the ionization front yet. Left: standing Alfvén wave, 2nd column: linearly polarized Alfvén wave, 3rd column: circularly polarized Alfvén wave, right: sound wave

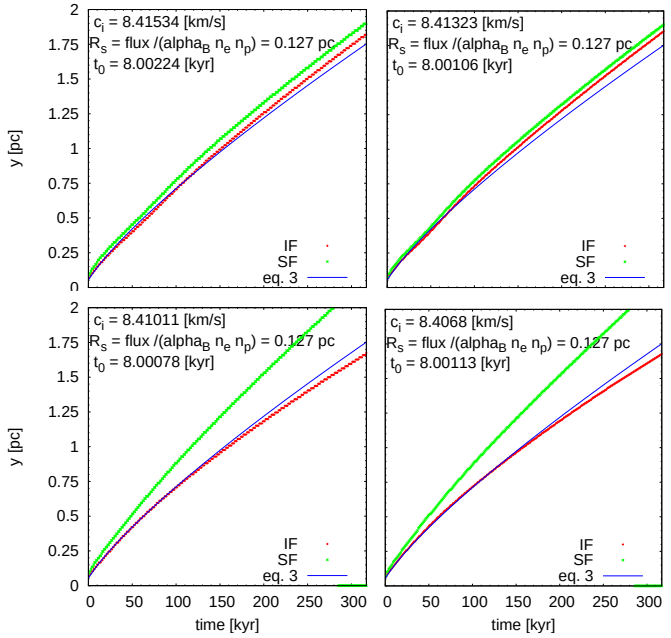

Fig. 2. Position of the ionization front. The blue line indicates the analytic solution (eq. 11), the position of the simulated ionization front is shown in red and the position of the shock front is shown in green. In the upper plots, no magnetic field is applied. Comparing the run with standard resolution (left) to the run with double resolution (right), shows that the shock width is set by numeric diffusion, whereas a background magnetic field of (bottom row) 10 μG causes a widening of the shock because due to the Alfvén velocity information can propagate into the cloud faster than the ionization travels that is slowed down by the swept up material.

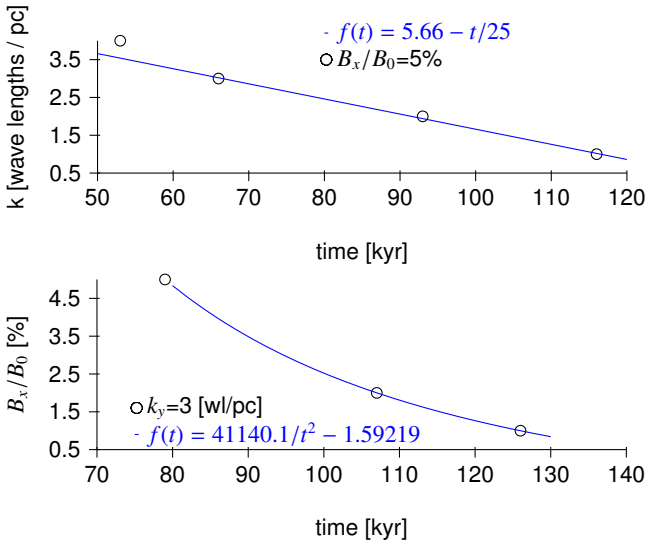

Fig. 3. Standing linear wave - bend off time

the ionizing radiation from the star. For plane parallel radiation $R_{\mathrm{Strömgren}}$ is given by

$$R_{\mathrm{Strömgren}} = \frac{f[\mathrm{photons/cm^2/s}]}{\alpha[\mathrm{cm^3/s}] n_e[1/\mathrm{cm^3}] n_p[1/\mathrm{cm^3}]} \quad . \tag{10}$$

A photon flux (f) of 10^9 [photons/cm^2/s], a density of 100 electrons and 100 protons per unit volume and the case B recombination coefficient (2.6×10^{-13} cm^3/s) lead to $R \sim 0.125$ pc which is in agreement with the simulations (approx. 10 percent of the box are ionized immediately).

When the ionization front reaches $R_{\mathrm{Strömgren}}$ the R-type ionizing front is converted to a D-type front and analogous to the derivation in Shu (1992) one can show that the plane parallel case leads to:

$$\frac{R(t)}{R_{\mathrm{Strömgren}}} \sim \left[1 + \frac{5}{4}\frac{c_i}{R_{\mathrm{Strömgren}}}(t - t_0)\right]^{4/5} \tag{11}$$

$$v(t) \sim \frac{c_i}{\sqrt[5]{1 + \frac{5}{4}(t - t_0)\frac{c_i}{R_{\mathrm{Strömgren}}}}} \tag{12}$$

with

$v(t)$	velocity of the ionization front
$R(t)$	location of the ionization front
t_0	time of the R/D type transition
c_i	sound speed, ionized medium [cm/s]

Perturbations and magnetic fields slow down the ionization front, but still Shu's approximation fits the position of the ionization front well.

If the molecular cloud is magnetized, the high Alfvén speed leads to a widening of the shock (fig. 2). The position of the shock front (SF) can also be found with Shu's approximation, since the distance between the IF and the SF is set by the speed of the fast magneto-sonic wave (eq. 9).

Since the magnetic field is parallel to the shock front, the speed of the fast magneto-sonic wave is

$$\frac{\omega}{k} = v_a^2 + c_s^2 \quad , \tag{13}$$

and the shock width is proportional to $\frac{B}{\sqrt{4\pi\rho}}$ (since $v_a \gg c_s$). If the magnetic field is only 1 μG the shock width is similar to the field free case and set by numerical diffusion.

3.2. Medium with density perturbations

If *only* the density is perturbed (not T) the system is no longer in pressure equilibrium. Consequently, the overdensity will diffuse. Setting an initial temperature perturbation to re-establish the pressure equilibrium will not solve this problem, because the code cools efficiently. But since the dense blobs diffuse with the initial sound speed of the dense medium (0.2 km/s) the crossing time for a knot with a radius of 1/12 pc is 0.8 Myr. The shock front only needs approx 0.3 Myr to cross the MHD box (box length = 2 pc) and the blobs are placed near the initial Strömgren radius - thus the diffusion of the blobs is not problematic.

Overdense regions will be ionized later and create molecular pillars lagging behind the ionization front in the unperturbed regions, which can be fit with Shu's approximation.

To excite a sound wave inside the molecular cloud, not only the density was perturbed but a sinusoidal perturbation was added to density and pressure.

$$\rho = \rho_0 + p\rho_0 \sin\left(k_y y\right) \tag{14}$$

$$E = E_0 + pE_0\gamma/(\gamma-1) \sin\left(k_y y\right) \tag{15}$$

p	size of the perturbation [fraction of ρ_0]
ρ	density [g/cm^3]
ρ	density in the homogeneous case
E	energy
E_0	energy in the homogeneous case

3.3. Standing linear Alfvén wave

If one perturbs the MHD equations and takes into account linearized hydromagnetic disturbances, the zero frequency case, ω=0, leads to a "simple" standing Alfvén wave. This kind of waves can be excited by introducing a small perpendicular sinusoidal perturbation without time dependence (ω=0) in the magnetic field. In our setup the unperturbed magnetic field is along y, thus we perturb the x-component of the magnetic field:

$$B_x = pB_y \sin\left(k_y y\right) \tag{16}$$

with

$B_{[xyz]}$	components of the magnetic field vector [Gauss/ $\sqrt{4\pi}$]
p	size of the perturbation [fraction of B_y]
ρ	density [g/cm^3]

and assume that the gas in the molecular cloud is at rest and has homogeneous density and pressure.

If *only* the B_x component of the magnetic field is perturbed the system is no longer in pressure equilibrium and the magnetic pressure gradient leads to a force in y-direction:

$$\nabla \frac{B_x^2}{8\pi} = p^2 B_y^2 k \sin\left(k_y y\right)\cos\left(k_y y\right) \quad . \tag{17}$$

This pressure gradient force ($\frac{1}{\rho}\nabla P_M$) in y direction is nothing else but the $(\nabla \times \boldsymbol{B}) \times \boldsymbol{B}$ term in the MHD equations. But intuitively this force that causes the acceleration of gas towards the nodes of the wave (and the overdensity at the nodes) is analogous to how wind is produced. Initially the gas pressure ($\rho c_s^2/\gamma = 9.36 \times 10^{-14}$[g/cm/s^2]) is lower than the magnetic pressure ($B_0^2/(8\pi) = 3.98 \times 10^{-12}$[g/cm/s^2]) and of the same order as the pressure caused by the perturbation ($B_x^2/(8\pi) = 0.99 \times 10^{-14}$[g/cm/s^2] for a 5% perturbation of B_0.)

The growth of the overdensities caused by the magnetic pressure gradient is proportional to kB^2 and is expected to stop as soon as the gas pressure of the overdense regions is able to balance the magnetic pressure gradient. Cooling of the gas lowers the gas pressure in dense regions delays the saturation.

If the amplitude grows in time proportional to kB^2 (which one would expect due to the pressure gradient), a given overdensity, (for example $\rho/\bar{\rho} = 1.1$) will be reached at a certain "bend off time". This "bend off time" (t_{BendOff}) is related to B^2 and k via $\rho/\bar{\rho} \propto kB^2 t_{\mathrm{BendOff}}$ or $t_{\mathrm{BendOff}} \propto 1/(B^2 k)$. The simulation also shows this proportionality (see fig. 3).

Since regions with similar (over)density but opposite orientation of the magnetic field become over or under-dense (depending on the orientation of the magnetic field) because magnetic tension pulls or pushes it, the magnetic field is more important for the build up of the dense regions than the density enhancements. This is obvious if one compares the energies in the magnetic field and the overdense region at early times (ratio of magnetic pressure to the pressure of the neutral gas) at later times the pressure of the hot, ionized gas ($nk_BT = n[1/\mathrm{cm}^3] \times 1.38 \times 10^{-12}$[gcm^2/s^2]) wins over magnetic pressure.

3.4. Propagating linear Alfvén wave

Linear Alfvén waves have a perturbation in the velocity and magnetic field component perpendicular to the magnetic field.

$$B_x = pB_y \sin\left(k_y y\right) \tag{18}$$

$$v_x = -pB_y/\sqrt{\rho} \sin\left(k_y y\right) \tag{19}$$

$B_{[xyz]}$	components of the magnetic field vector [Gauss/ $\sqrt{4\pi}$]
$v_{[xyz]}$	components of the gas velocity [km/s]
p	size of the perturbation [fraction of B_y]
ρ	density [g/cm^3]

Again the perturbation of the field strength leads to a pressure gradient force along y. Basically the perturbation of the magnetic field leads to the same situation as discussed for the standing Alfvén wave.

The magnetic perturbation causes a force like

$$\frac{1}{\rho}\nabla P_M = B_0^2/\sqrt{\rho} k \cos(ky0)\sin(ky) \quad . \tag{20}$$

But since there is also a perturbation of the momentum, this causes a force like

$$\partial M_x/\partial t \propto \sin(\text{Alfven oscillation period}) \quad . \tag{21}$$

The net force creates propagating nodes, which can be observed as moving dense knots (secondary maxima) in the simulation.

After full oscillation cycles, there should be no density perturbation left. During the oscillation the changes in density should be small and unimportant, but still present. Fig. 4 shows that the density perturbations are indeed much smaller than in the standing Alfvén wave, but don't vanish after full cycles. This is probably caused by cooling.

3.5. Circularly polarized Alfvén wave

A circularly polarized Alfvén wave consists of two superposed linear Alfvén waves with phase shift:

$$B_x = pB_y \sin\left(k_y y\right) \tag{22}$$

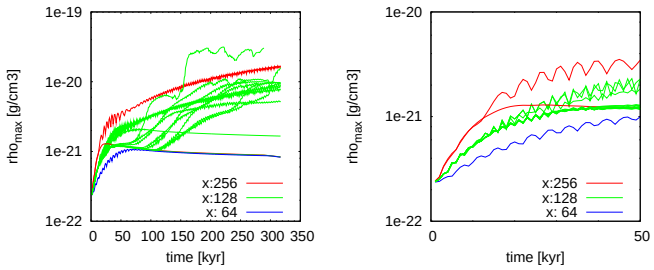

Fig. 5. Color coded: as long as the shock has not widened yet, the maximal density depends only on the resolution in x - direction.Similar colors indicate similar resolution. The second plot is a zoom.

$$B_z = pB_y \cos\left(k_y y\right) \quad (23)$$

$$v_x = -pB_y/\sqrt{\rho}\sin\left(k_y y\right) \quad (24)$$

$$v_z = -pB_y/\sqrt{\rho}\cos\left(k_y y\right) \quad . \quad (25)$$

The difference between this setup and the linear Alfvén waves is, that this magnetic field perturbation does not lead to a net force ("force free magnetic field") :

$$\begin{aligned}\nabla P_M &= 0.5B_0^2\nabla(1 + kp(\sin^2(ky) + \cos^2(ky))) \\ &= 0.5B_0^2\nabla(1 + kp) = 0 \quad . \end{aligned} \quad (26)$$

This should not create density enhancements since there is no net force and fig. 4 shows that density fluctuations in cells, that are not reached by ionizing radiation yet, are only at the level of machine precision.

Inside the shock density enhancements with one maximum per wavelength start building up. The maxima are distorted and propagating.

4. Discussion

In this section the different seeds for pillars are compared. The aims of the simulations described above were (1) finding the smallest seed that leads to molecular pillars with realistic orientation and (2) investigating if different types of seeds show the same conditions for star formation at their tips. For this scaling study perturbations with various wavelengths as well as different strengths and orientations of the B-field were used.

4.1. Evolution of the density maxima

In all simulations the cells with the hightest density are located near the ionization front. The evolution of this maximal density can be caracterized using four different stages: a "rise" depending on the resolution in x - direction (subsect. 4.1.1), a "knee" and slope depending on the Alfvén speed (subsect. 4.1.3), a "rise" proportional to the resolution in y - direction (subsect. 4.1.3) and a saturation value (subsect. 4.1.4).

4.1.1. "Rise" proportional to x resolution

In early phase of the simulation, the shock is not resolved yet and all swept up medium is piled up in one cell (see fig. 5). Consequently the maximal density depends on the resolution in x direction.

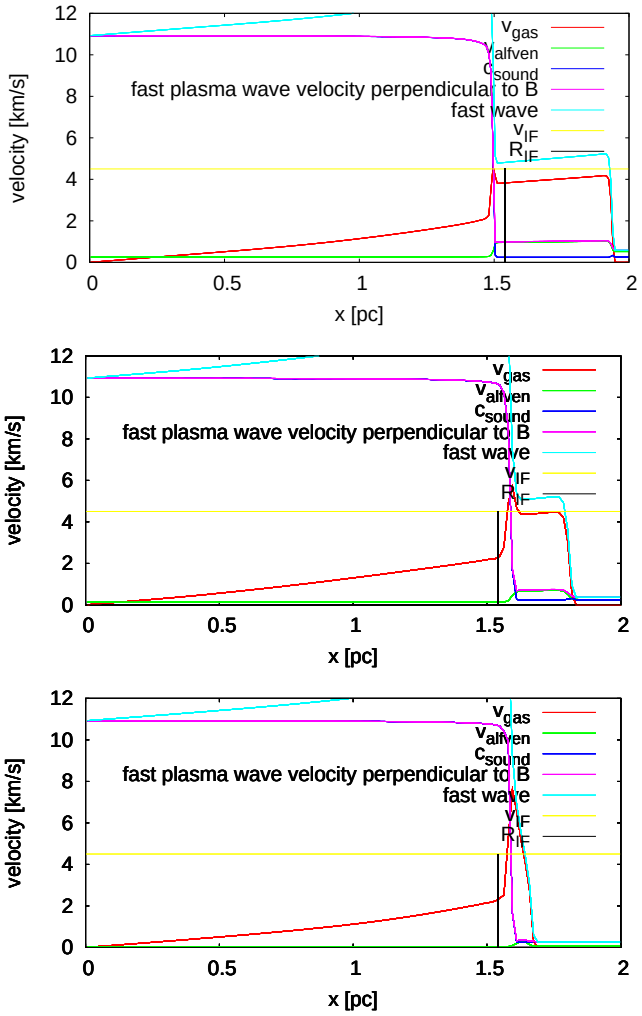

Fig. 6. Simulations show that the distance between the ionization front (IF) and the shock front (SF) scales with the magnetic field strength resp. the Alfvén velocity. The velocities of different wave families are plottet for a background field of $10\,\mu$G (top), $5\,\mu$G (middle) and $1\,\mu$G (bottom). The yellow line indicates the expected position of the ionization front in the field free case.

4.1.2. "Knee" and slope depend on the Alfvén speed

If a magnetic field is present, the fast Alfvén wave (eq. 9) can be fast enough that the shock can widen. Also in the nonmagnetic case, numerical diffusion leads to a widening of the shock. As soon as the width of the shock is more than one cell the maximal density starts getting smaller. The velocity of a one dimensional ionization front is $c_s/\sqrt[3]{1 + 1.25c_s/R_s(t - t_0)}$. It starts with approx 8.4 km/s and reaches approx. 4 km/s after 300 kyr. The sound speed (c_s) is 0.2 km/s. The Alfvén speed (v_A) for 10 micro Gauss is 2 km/s. Thus, the velocity of the fast magneto-sonic wave is similar to v_A in this case.

The distance between the ionization front (IF) and the shock front (SF) therefore scales with the magnetic field strength (B). Simulations (fig. 6) show that (SF-IF) in the 5 micro Gauss case is only half the (SF-IF) in the 10 micro Gauss case. If the background magnetic field is only 1 Microgauss, this leads to an Alfvén velocity below the sound speed. Hence the shock does not widen enough and the maximal density does not show a "knee" and its slope only changes due to numerical diffusion.

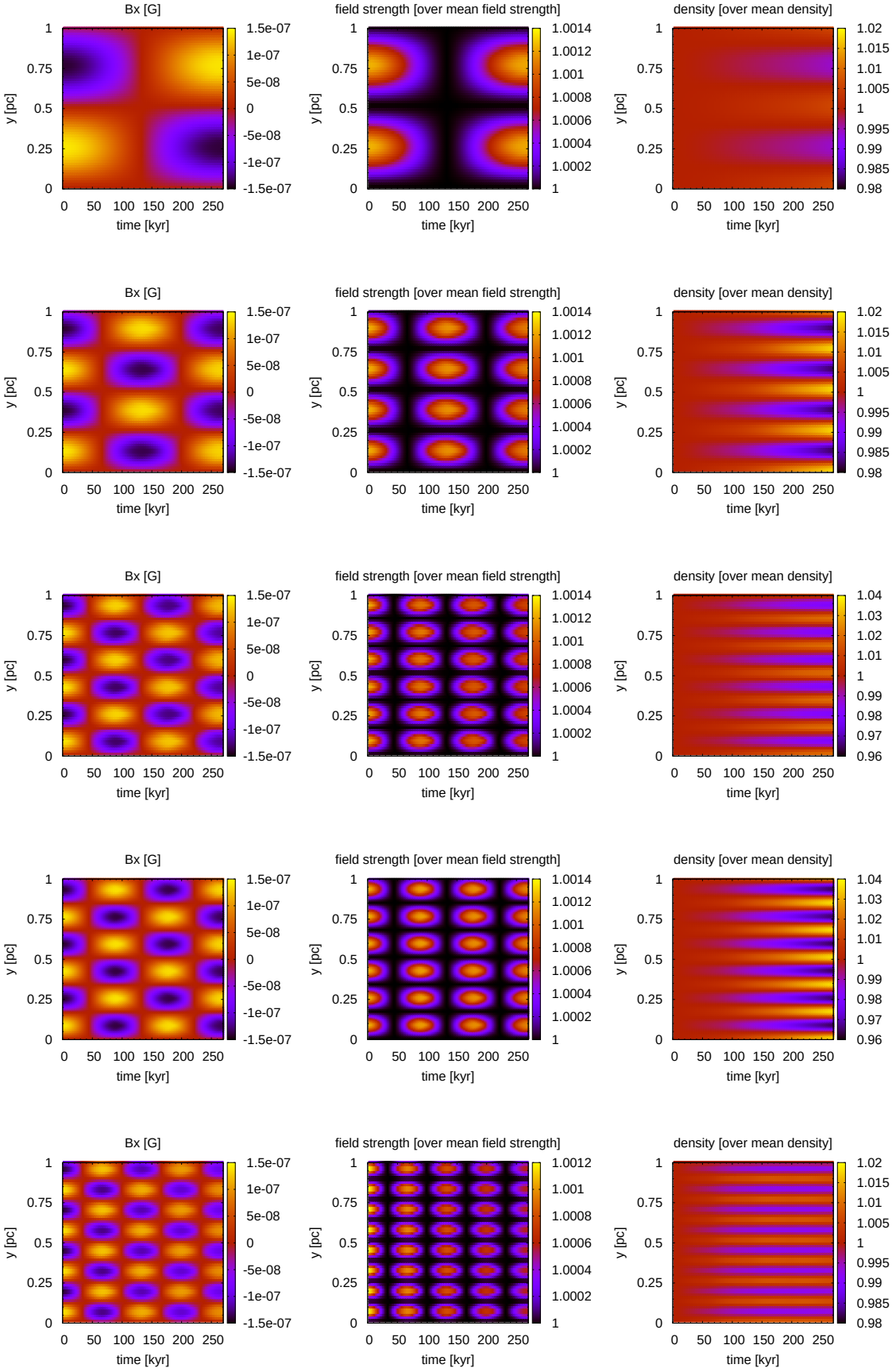

Fig. 9. Time evolution of one column (x,z fixed) of cells that are not reached yet by the shock.

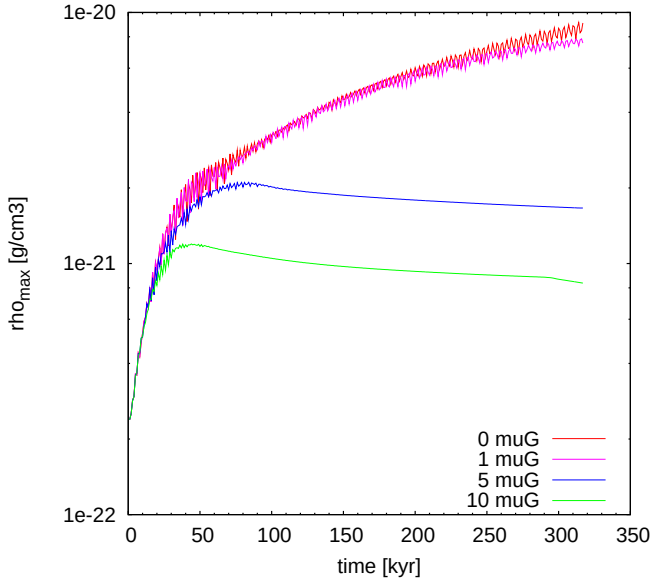

Fig. 7. Dependence of the maximal density on the field strength

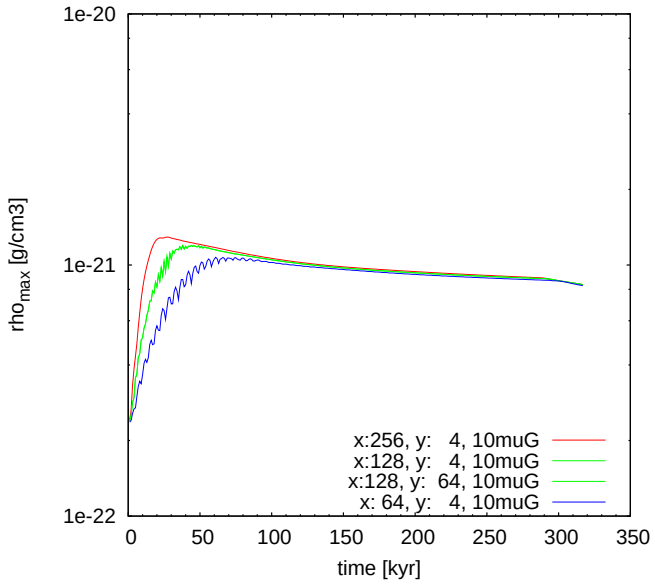

Fig. 8. Convergence of the simulations with a homogeneous magnetic field.

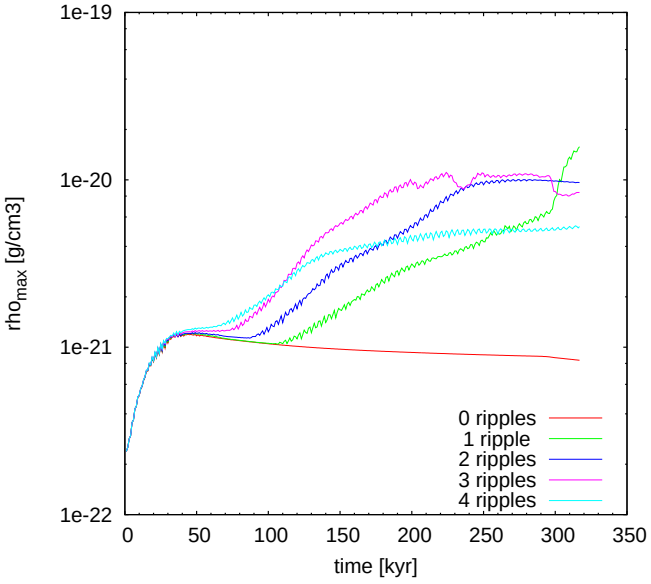

Fig. 10. Dependence of the evolution of the max. density on the wavelength of the perturbation.

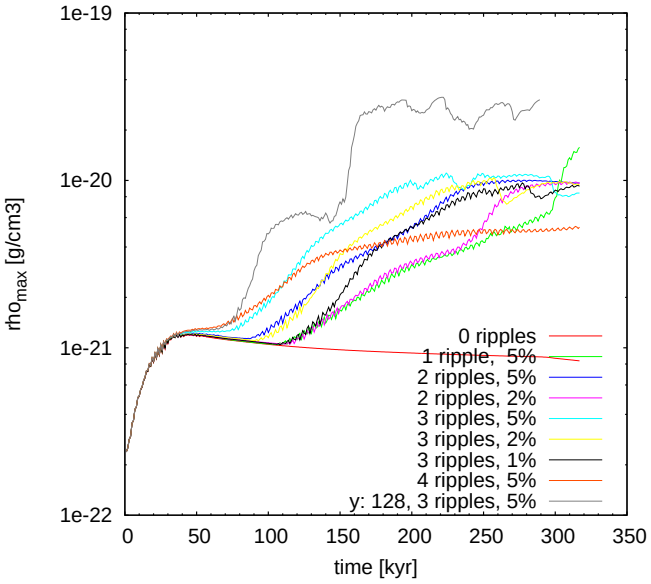

Fig. 11. Dependence of the evolution of the max. density on the amplitude of the perturbation.

Due to the latter the maximal density in simulations with twice the standard resolution rises (a factor 2) faster than the the maximal density in simulations with the standard resolution and reaches the "knee" faster.

The run with half the field strength reaches the "knee" later and at higher densities (fig. 7).

All simulations with a homogeneous magnetic field converge to the same density (after the knee) independent of the resolution in x and y (fig. 8).

The velocity of the Alfvén wave is fastest perpendicular to the shock (at the minimum or maximum of the standing wave). This leads to a rippled shock. The sinusoidal perturbation of the x-component of the magnetic field $B = (B_0 \Delta \sin(ky), B_0, 0)$ leads to standing Alfvén waves.

This can be seen in fig. 9. In these plots the time evolution of one column (x,z fixed) of cells that are not reached yet by the shock is shown.

4.1.3. "Rise" proportional to y resolution

In simulations with density inhomogeneities created by the perturbations seeded into the molecular cloud (Alfvén waves, sound wave) a second phase of rapid growth of the maximum density

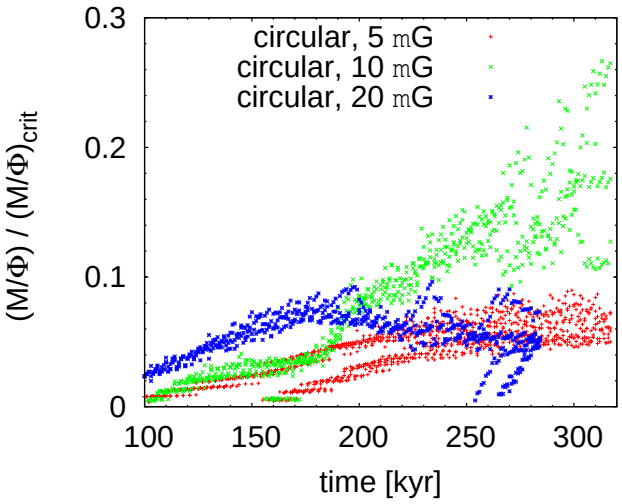

Fig. 14. Stabilization of overdense regions by the magnetic field: impact of the background field. All simulations used Alfvén waves with an amplitude of 5% of the background field.

can be observed. Higher wave numbers (fig. 10) and higher amplitudes (fig. 11) of the B_x perturbation lead to an earlier rise. The "four ripple" case reaches the saturation value very early because it is under-resolved (see saturation value).

4.1.4. Saturation value

In late stages of the simulation, the maximum density saturates. The saturation value depends on the number of cells per wavelength: the resolution in y direction and the wave number. The overdensity got swept up until the density peaked in a single cell. If fewer cells or higher wave numbers are used, this happens earlier and at lower density.

4.2. Stabilizing effect of the magnetic field

Tomisaka et al. (1988) found numerically that the asymptotic value for the maximal mass of a spherical cloud which can still be supported by a given magnetic field is

$$M_{\rm cloud} = 0.12 \frac{\Phi_{\rm B}}{\sqrt{G}} \quad . \tag{27}$$

Where M is the cloud mass in grams, and $\Phi_{\rm B} = \pi R^2_{\rm cloud} B_0$ is the magnetic flux ancored in the cloud.

Fig. 12 shows this mass to flux ratio (M/Φ) for overdense regions in the simulations with Alfvén waves. These regions were defined as regions in which the density in each cell is a factor 10 higher than the initial density. All structures shown in this plot have mass to flux rations below one and are thus hostile to star formation since the magnetic field is strong enough to stabilize all of them.

4.3. Orientation of the pillars

The heads of the pillars caused by standing Alfvén waves always point towards ionizing radiation source, just like the heads of the observed pillars. The pillars created by the linearly and circularly polarized Alfvén wave are superpositions of two components. A component similar to the standing Alfvén wave and a component propagating in y direction. Thus the heads of these pillars don't always point exactly towards ionizing radiation source but rather wobble around this position. Fig. 13 shows a snapshot of the pillars after 300 Myr.

4.4. Orientation of the magnetic field

Sugitani et al. (2007) reported on imaging polarimetry in the Eagle nebula that showed, that the pillars are found in regions in which the magnetic field does not follow the global field pattern but is rather aligned with the pillars.

It is an interesting "chicken & egg" problem whether the magnetic field in the elephant trunks is aligned with the molecular pillars because the gas dragged along the field lines or if the magnetic pressure of wiggly field lines just sweeps the gas into these regions.

In our simulations the overdense regions are created by magnetic pressure at the nodes of the Alfvén waves. The field does not follow the global pattern in the dense regions (fig. 13) and the largest x-component of the magnetic field is found at the position of the pillars. However, the field direction is not along the pillar, because the background magnetic field was oriented in y-direction and is still stronger than x and z component of the magnetic field vector.

5. Conclusions

Our simulations showed that Alfvén waves can indeed create magnetic pillars. Pillar creation in our simulation does not depend on initial density perturbations, but non force free fields (standing + linearly polarized Alfvén waves) create density perturbations automatically (fig. 4). In the case of a circularly polarized wave the overdensity should vanish after full cycles. However, since cooling is more efficient in dense regions the passing wave leaves a permanent imprint in the gas. Also the energy stored in an Alfvén wave is much larger than the energy stored in turbulent velocities or sound waves with the same amplitude.

The magnetic flux to mass ratio showed that the case with three wavelengths per parsec and a background field of $10\,\mu$G seems to be an exceptional setup: here the simulation created pillars that were more prone to star formation than simulations with shorter/longer wavelengths and higher/lower background fields (fig. 12 and 14).

The pillars in our simulations are not well resolved. A series of CPU-intensive re-simulations with enhanced resolution is currently being performed to better resolve the structure of the pillars.

Acknowledgements. This research was supported by the ISIMA program (fellowships for KMF and MG) and the *Deutsche Forschungsgemeinschaft, DFG* cluster of excellence *Origin and Structure of the Universe* (`www.universe-cluster.de`). We thank J. Stone for usefull discussions.

References

Billot, N., Noriega-Crespo, A., Carey, S., et al. 2010, ApJ, 712, 797
Carlqvist, P., Gahm, G. F., & Kristen, H. 2003, A&A, 403, 399
Deharveng, L., Zavagno, A., & Caplan, J. 2005, A&A, 433, 565
Deharveng, L., Zavagno, A., Schuller, F., et al. 2009, A&A, 496, 177
Elmegreen, B. G., Kimura, T., & Tosa, M. 1995, ApJ, 451, 675
Gardiner, T. A. & Stone, J. M. 2005, Journal of Computational Physics, 205, 509
Gardiner, T. A. & Stone, J. M. 2008, Journal of Computational Physics, 227, 4123
Gritschneder, M., Naab, T., Burkert, A., et al. 2009a, MNRAS, 393, 21
Gritschneder, M., Naab, T., Walch, S., Burkert, A., & Heitsch, F. 2009b, ApJ, 694, L26

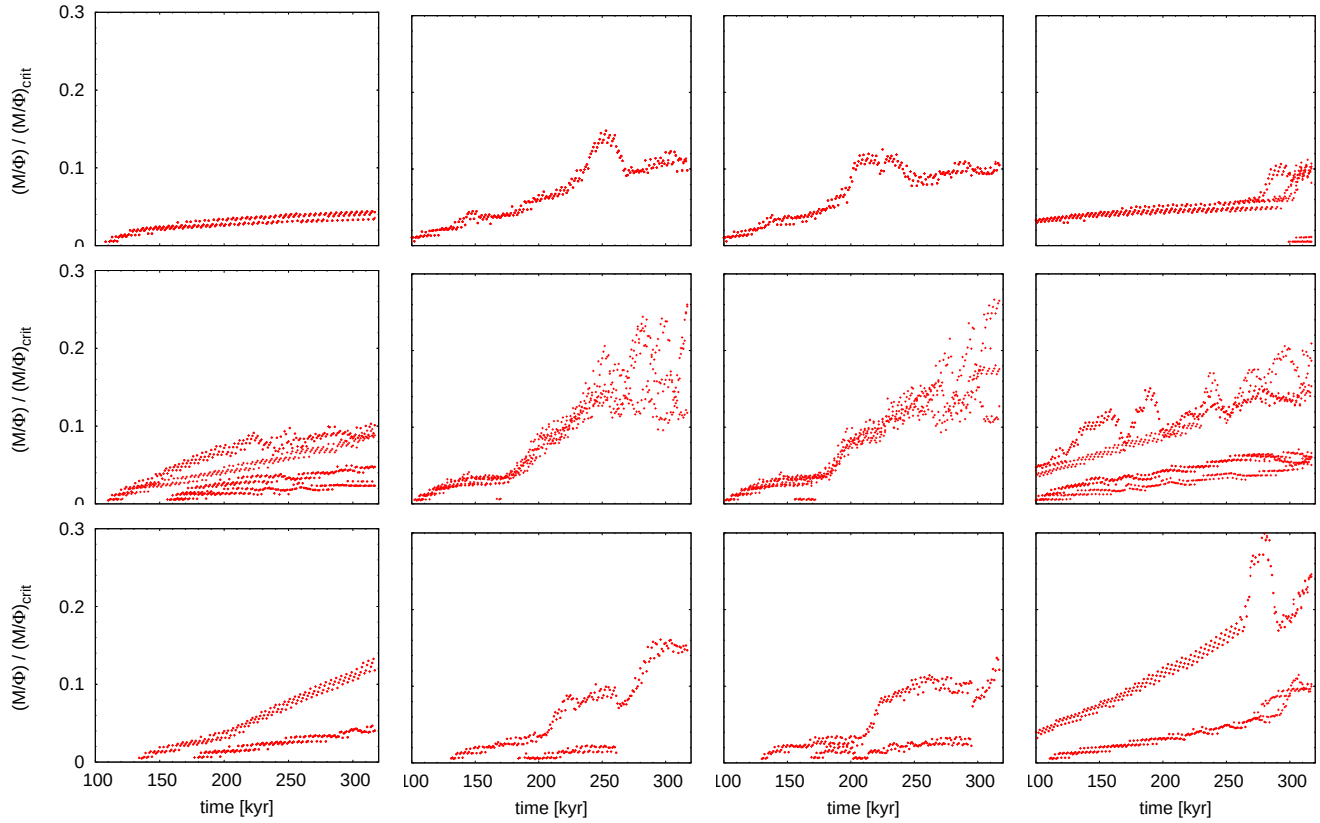

Fig. 12. Stabilization of overdense regions by the magnetic field. Left: standing Alfvén wave, 2nd column: linearly polarized Alfvén wave, 3rd column: circularly polarized Alfvén wave, right: sound wave. Top: 4 wave lengths, middle: 3 wave lengths, bottom : 2 wave lengths

Guarcello, M. G., Micela, G., Peres, G., Prisinzano, L., & Sciortino, S. 2010, ArXiv e-prints
Henney, W. J., Arthur, S. J., de Colle, F., & Mellema, G. 2009, MNRAS, 398, 157
Ikeda, H., Sugitani, K., Watanabe, M., et al. 2008, AJ, 135, 2323
Koyama, H. & Inutsuka, S. 2002, ApJ, 564, L97
Krumholz, M. R., Stone, J. M., & Gardiner, T. A. 2007, ApJ, 671, 518
Li, H., Blundell, R., Hedden, A., et al. 2010, ArXiv e-prints
Price, D. J. & Bate, M. R. 2010, in American Institute of Physics Conference Series, Vol. 1242, American Institute of Physics Conference Series, ed. G. Bertin, F. de Luca, G. Lodato, R. Pozzoli, & M. Romé , 205–218
Redman, M. P., Williams, R. J. R., Dyson, J. E., Hartquist, T. W., & Fernandez, B. R. 1998, A&A, 331, 1099
Shu, F. H. 1992, The Physics of Astrophysics, Vol. II, The Physics of Astrophysics, Volume II, Gas dynamics (University Science Books)
Smith, N., Povich, M. S., Whitney, B. A., et al. 2010, MNRAS, 406, 952
Stanke, T., Smith, M. D., Gredel, R., & Szokoly, G. 2002, A&A, 393, 251
Stone, J. M. & Gardiner, T. 2009, New Astronomy, 14, 139
Stone, J. M., Gardiner, T. A., Teuben, P., Hawley, J. F., & Simon, J. B. 2008, ApJS, 178, 137
Sugitani, K., Tamura, M., Nakajima, Y., et al. 2002, ApJ, 565, L25
Sugitani, K., Watanabe, M., Tamura, M., et al. 2007, PASJ, 59, 507
Tomisaka, K., Ikeuchi, S., & Nakamura, T. 1988, ApJ, 335, 239
Walborn, N. R., Maíz-Apellániz, J., & Barbá, R. H. 2002, AJ, 124, 1601
Ward-Thompson, D., Nutter, D., Bontemps, S., Whitworth, A., & Attwood, R. 2006, MNRAS, 369, 1201
Williams, R. J. R. & Dyson, J. E. 2001, MNRAS, 325, 293
Williams, R. J. R., Dyson, J. E., & Hartquist, T. W. 2000, MNRAS, 314, 315
Zhao, J., Morris, M. R., Goss, W. M., & An, T. 2009, ApJ, 699, 186

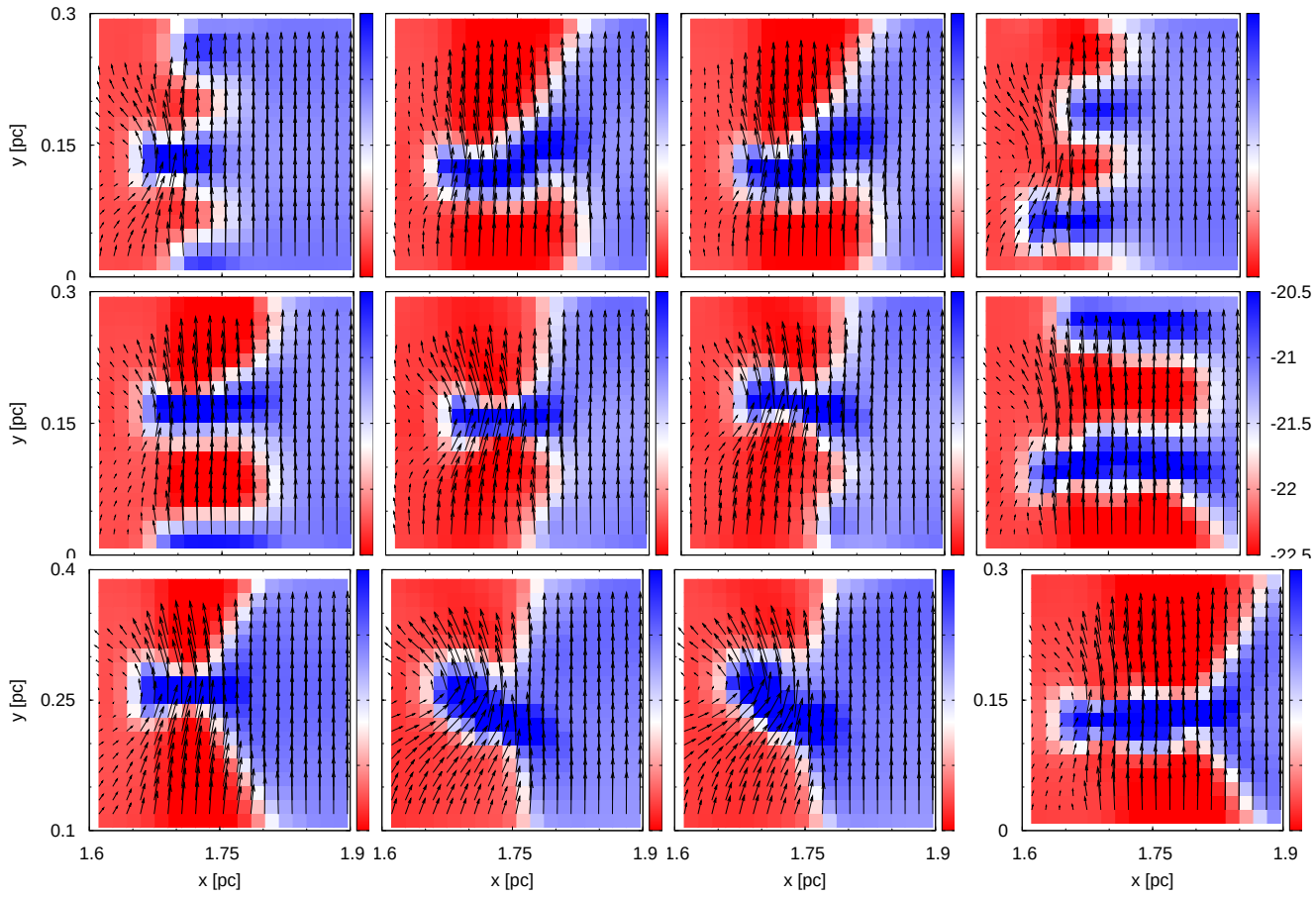

Fig. 13. Orientation of the magnetic field. color coded: $\log \rho$ [g/cm^3], arrows: magnetic field vectors. Left: standing Alfvén wave, 2nd column: linearly polarized Alfvén wave, 3rd column: circularly polarized Alfvén wave, right: sound wave. Top: 4 wave lengths, middle: 3 wave lengths, bottom : 2 wave lengths